Electronic Supporting Information for

Thermally activated LTA(Li)-Ag zeolites with water-responsive photoluminescence properties

Eduardo Coutino-Gonzalez,[a] Wouter Baekelant,[a] Didier Grandjean,[b] Maarten B.J. Roeffaers,[c] Eduard Fron,[a] Mohammad S. Aghakhani,[b] Nicolas Bovet,[d] Mark Van der Auweraer,[a] Peter Lievens,[b] Tom Vosch,[d] Bert Sels[*c] and Johan Hofkens[*a]

[a]Division of Molecular Imaging and Photonics, Department of Chemistry, K.U. Leuven, Celestijnenlaan 200F, 3001 Leuven, Belgium. Email: johan.hofkens@chem.kuleuven.be

[b]Laboratory of Solid State Physics and Magnetism, Department of Physics and Astronomy, K.U. Leuven, Celestijnenlaan 200D, 3001 Leuven, Belgium.

[c]Centre for Surface Chemistry and Catalysis, Department of Microbial and Molecular Systems, K.U. Leuven, Kasteelpark Arenberg 23, 3001 Leuven, Belgium. Email: bert.sels@biw.kuleuven.be

[d]Nano-Science Center, Department of Chemistry, University of Copenhagen, Universitetsparken 5, 2100 Copenhagen, Denmark.

*Corresponding author: johan.hofkens@chem.kuleuven.be, bert.sels@biw.kuleuven.be

S1. Scanning electron microscope (SEM) images, structural formula and composition of the zeolites used in this study.

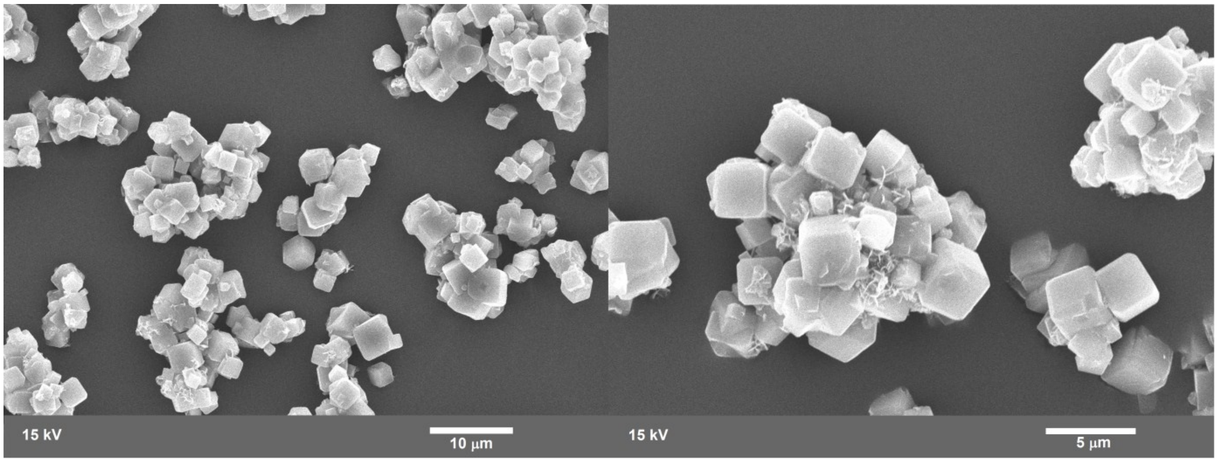

Figure S1. SEM images of the starting materials used in this study, LTA in its Na form partially exchanged with Li ions. The crystals with an average size distribution between 3 to 5 µm present a cubic shape with truncated edges. The images were recorded using non-coated samples on a JEOL-6010LV SEM.

LTA zeolites used in this study have a silicon to aluminum (Si/Al) ratio of 1 and the following structural formulas.

Table S1. Chemical composition of a hydrated unit cell of the zeolite used in this study.

Zeolite	**Structural formula**
LTA(Na)	$|Na^+_{96}|$ $[Al_{96}Si_{96}O_{384}]$ $|H_2O|_{216}$
LTA(Na)[a]	$|Na^+_{12}|$ $[Al_{12}Si_{12}O_{48}]$ $|H_2O|_{27}$
LTA(Li)[b]	$|Na^+_8Li_4^+|$ $[Al_{12}Si_{12}O_{48}]$ $|H_2O|_{27}$

a. After normalization of the T atoms of the unit cell to 24. b. Elemental analysis of the LTA(Li) zeolite, measured by XPS, showed a Si/Al ratio close to one and a Li/Na ratio of about 0.5. These results were further corroborated by ICP-AES analysis where a Si/Al ratio of 1.04 and a Li/Na ratio of 0.58 were obtained.

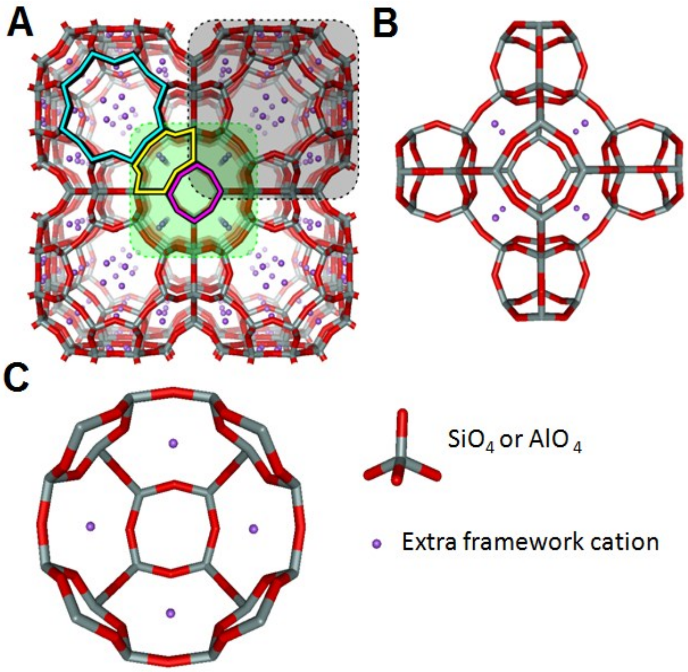

Figure S2. Schematic representation of A) LTA unit cell displaying the sodalite (green dashed area) and super cage (gray dashed area); the S8R, S6R, and S4R rings are highlighted in cyan, yellow and pink, respectively, B) isolated sodalite cage showing the S4R connectors, and C) transversal section of a sodalite cage.

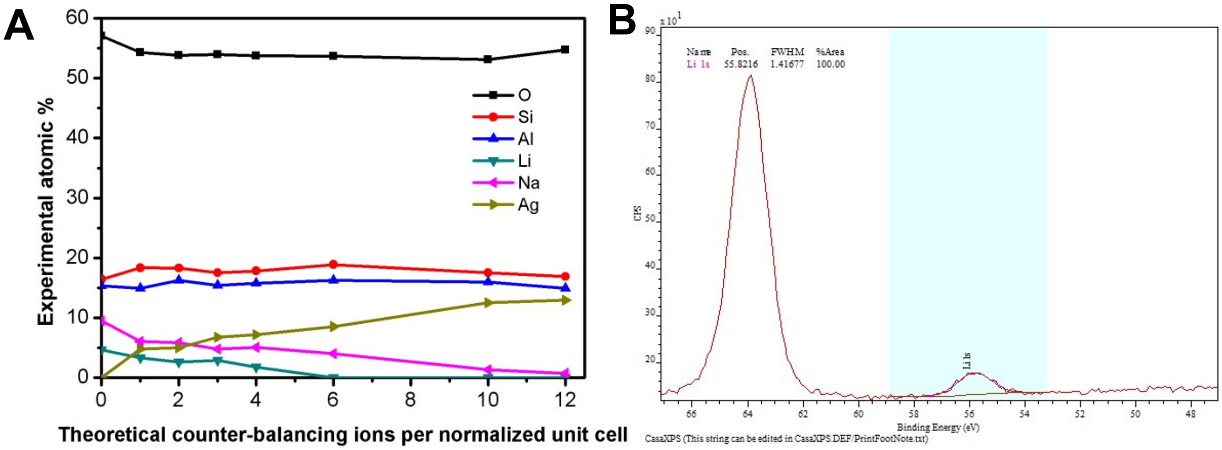

Figure S3. A) Atomic percentage survey, measured by XPS, of the different elements present in the LTA(Li)-Ag composites as a function of the theoretical number of counter-balancing cations per normalized unit cell. B) XPS spectrum showing the Li 1s peak (around 56 eV) and Na 2s peak (around 64 eV), measured for LTA(Li).

From the elemental analysis performed by XPS and ICP on the LTA(Li) sample (Figure S3) we observed a Si/Al ratio close to one and a Li/Na ratio of about 0.5. In this study we followed the procedure described by Yahiro and coworkers[1] to fabricate LTA zeolites in its lithium form at bulk scales; they reported the synthesis of partially exchanged LTA(Li) samples with different Li/Na ratios (0.2, 0.7, and 2). Our results are in agreement with those previously described by Yahiro *et al*. However, we acknowledge the existence of other cation exchange protocols to obtain higher Li loadings in zeolites.[2,3] Nevertheless, in these protocols the cation exchange is performed at single crystal level using super saturated conditions (highly concentrated $LiNO_3$ solutions, high temperatures and pressure).

Further on during the Ag exchange, we observed a decrease of the Na and Li cations when Ag cations were exchanged in the sample. However, the exchange dynamics were different between Li and Na cations, a rapid decrease of Li cations was observed in samples containing intermediate silver loadings (Ag_1 - Ag_6), whereas in the sample containing six Ag cations per normalized unit cell about half of the Na cations were exchanged. From Ag_6 to Ag_{12} silver loadings, the remaining Na cations were exchanged by Ag cations. This trend is in line with the selectivity series (derived from the exchange isotherms) for LTA zeolites, which is as follows for univalent ions; Ag >>> Cs > Rb > K > Na > Li. Silver displays the highest selectivity, this is due to the large polarizability of silver compared to alkali ions. This means that a complete cation replacement is expected when silver ions are exchanged in LTA zeolites. Moreover, based on the same selectivity criteria, it is expected that Li ions will be the first ones to be exchanged by Ag, followed by Na ions. The atomic percentage of O, Si and Al atoms remained stable over the analyzed samples. The O atomic percentage on the samples was estimated around 57 % which is fully in agreement with the O atomic percentage in dehydrated LTA(Li) zeolites (57 %).

S2. Heating cell used for *in-situ* steady state luminescence measurements at different temperatures and schematic representation of the set-up employed for EQE measurements.

For the *in-situ* excitation-emission measurements at different temperatures we designed and built a heating cell (Figure S4), this device was coupled to an integrating sphere (Labsphere) which was connected to a fluorimeter (Edinburgh Instruments FLS 980) via optic fibers. The sample was pressed into 13 mm diameter pellets (1 mm thickness) using a mechanical press (1.5 tons), then mounted and hermetically sealed into the heating cell sample compartment by using a quartz plate (see Figure S4). After this, the sample was heated using a temperature ramp of 5 °C per minute, until the desired temperature was reached, then the sample was left at the measurement temperature for 1 hour for stabilization. After reaching the desired temperature the sample was cooled down under vacuum using a Pfeiffer turbo molecular pump (1 x 10^{-4} bar pressure). Excitation-emission measurements were performed at room temperature.

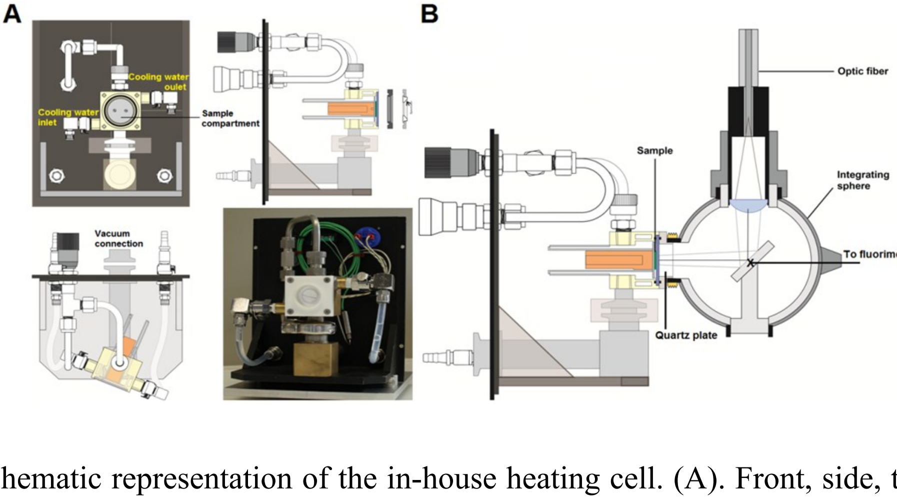

Figure S4. Schematic representation of the in-house heating cell. (A). Front, side, top & real view of the heating cell employed in this study. (B). Side view of the heating cell attached to the integrating sphere. The heating cell was built by the mechanical workshop of the KU Leuven.

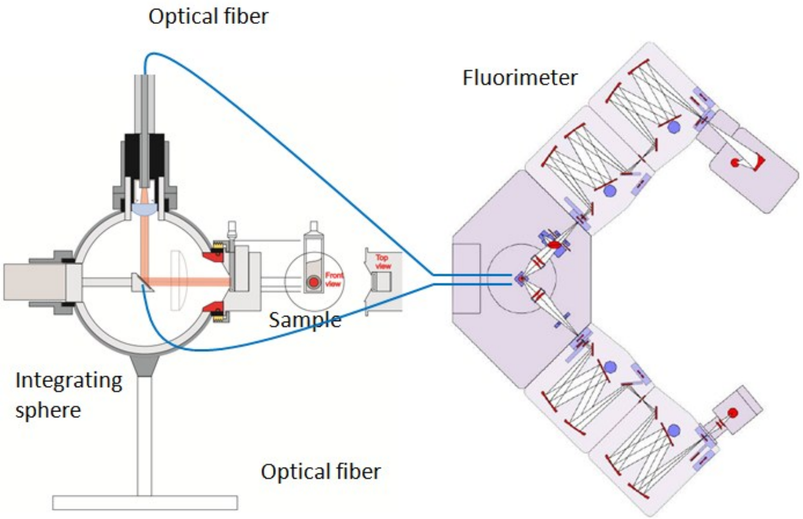

Figure S5. Schematic representation of the set-up utilized in this report to measure EQE values.

Table S2. External quantum efficiencies of LTA(Na)-Ag and LTA(Li)-Ag zeolites synthesized under the same conditions.

Silver content, x[‡]	External quantum efficiency (%)			
	LTA(Li)-Ag_x		LTA(Na)-Ag_x	
1	45.9 ± 1.3[a]	61.5 ± 2.1[b]	3.7 ± 1.1[a]	4.0 ± 1.2[b]
2	42.9 ± 2.2[a]	48.7 ± 1.4[b]	-	-
3	25.9 ± 1.9[a]	33.8 ± 2.8[b]	1.4 ± 1.0[a]	1.7 ± 1.3[b]
4	16.6 ± 1.7[a]	21.0 ± 1.7[b]	-	-
5	10.1 ± 2.5[a]	12.1 ± 2.5[b]	-	-
6	5.6 ± 1.4[a]	7.7 ± 1.6[b]	ND	ND

[‡]Where x denotes the number of silver atoms per normalized unit cell. [a]Using 260 nm as excitation wavelength. [b]Using 280 nm as excitation wavelength. ND = Non detectable values. Standard deviations were calculated based on an average of three measurements in three different batches (9 values in total). Two commercial phosphors ($BaMgAl_{10}O_{19}:Eu^{2+}$, $BaMgAl_{10}O_{19}:Eu^{2+},Mn^{2+}$) with known EQE's were measured and used as references for the calibration of the set-up.[4]

S3. Photoluminescence comparison between thermally treated LTA(Na)-Ag and LTA(Li)-Ag samples.

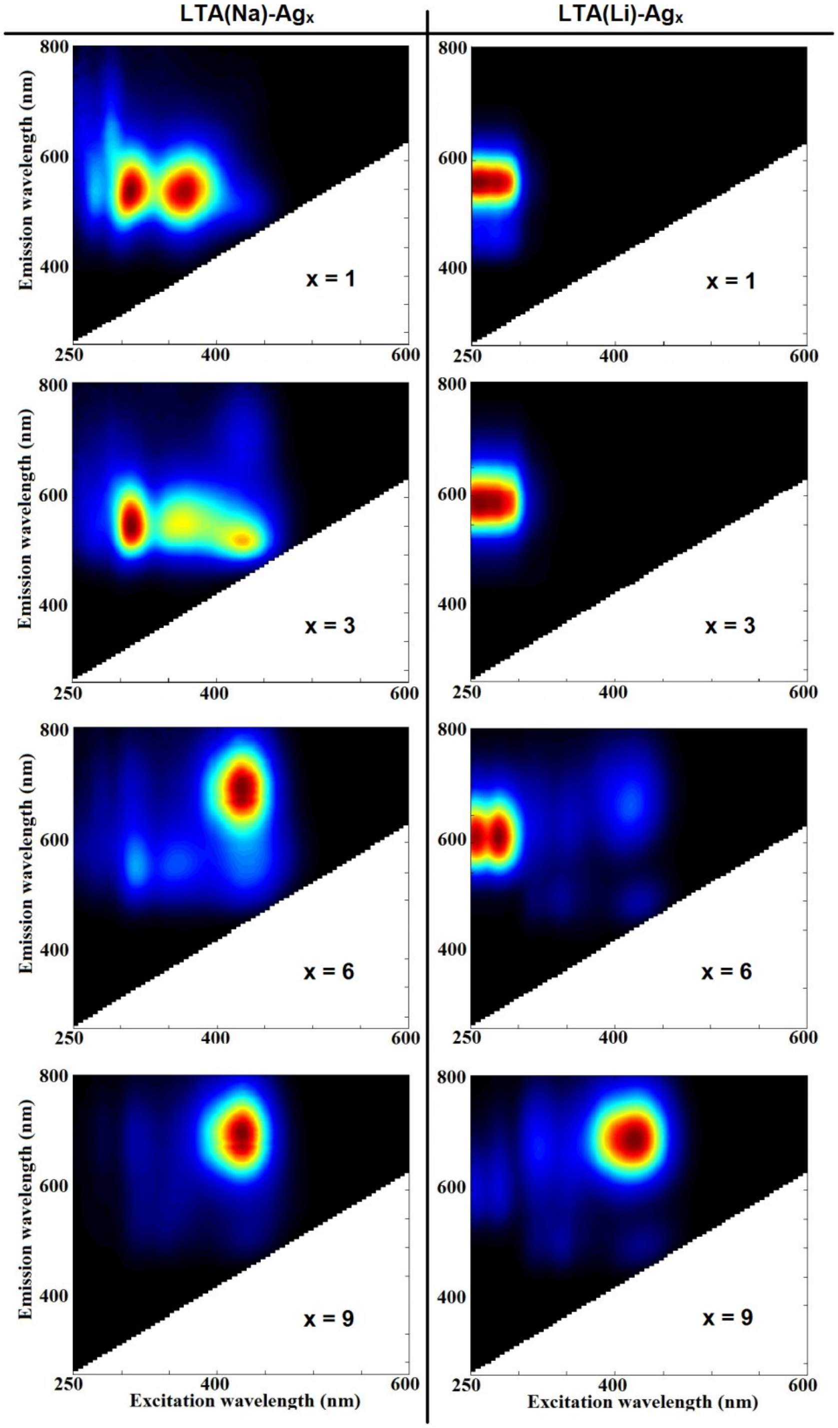

Figure S6. 2D excitation-emission plots of selected LTA(Na)-Ag and LTA(Li)-Ag samples, synthesized under the same conditions.

In Fig. S6 the 2D excitation-emission plots of selected LTA(Na)-Ag and LTA(Li)-Ag zeolites, in their fully hydrated state, is displayed for comparison. The formation of green, yellow, and red emitting Ag-zeolite composites was observed in LTA(Li)-Ag samples depending on their silver content. At low silver loadings, green emission is dominant for LTA(Li)-Ag_1. Yellow emission was found in sample LTA(Li)-$Ag_{3\text{-}6}$ and finally red emission was observed in samples with higher silver contents, LTA(Li)-$Ag_{9\text{-}12}$. The emission profiles of the luminescent LTA(Li)-Ag_1 composites (low silver loadings) are consistently blue shifted with 60 - 100 nm in excitation wavelength compared to the related LTA(Na)-Ag_1. At intermediate Ag loadings, a clear difference in the PL profiles between thermally treated LTA(Na)-Ag_6 and LTA(Li)-Ag_6 samples is visible. Yellow emission color (excited at 280 nm) was measured on LTA(Li)-Ag_6 zeolites whereas red emissive features were recorded on LTA(Na)-Ag_6 zeolites (420 nm excitation). When high silver loadings were employed an emission band with maxima between 680 and 700 nm appeared upon excitation at 420 nm in both LTA(Na)-Ag_9 and LTA(Li)-Ag_9 samples. Simultaneously a decrease of the emission band between 570 and 600 nm was observed.

S4. Thermogravimetric and FT-IR analysis of LTA(Li)-Ag zeolite composites. Thermogravimetric analysis was performed on a Q500 TGA device (TA instruments). Approximately 20 mg of heat-treated LTA(Li)-Ag zeolite composites were loaded in a platinum sample holder. The sample was heated using a temperature rate of 5 °C per minute to 650 °C under a constant nitrogen flow of 90 mL/min. We performed the analysis of the entire series of LTA(Li)-$Ag_{1\text{-}12}$ and the starting LTA(Li) zeolite. By using TGA the water content in zeolites can be studied as a function of temperature. Based on this analysis, we performed a correlation between the amount of water molecules and the luminescence behavior in LTA(Li)-Ag zeolites. Slight differences can be expected since the heating process carried in both analysis is not exactly the same. In the case of the *in-situ* luminescence analysis as a function of temperature, a partially stationary approach was employed, whereas in TGA a dynamic configuration was used. Nevertheless, we tried to keep the heating conditions (temperature rate, use of vacuum, gas flow) as similar as possible to obtain a close estimation of the correlation between both analysis.

The TGA profile of the LTA(Li)-Ag_1 composite (Figure S7) shows a water content of about 19 % in the fully hydrated sample. At 50 °C the water contents drops to 17 % corresponding to approximately 180 water molecules per normalized unit cell. As the temperature rises to 75, 100, 200, 300, and 400 °C, the calculated water molecules present in the normalized unit cell decrease to approximately 120, 50, 20, 10, and 3, respectively. Based on TGA experiments only 1 water molecule per normalized unit cell is expected for samples treated at 450 °C.

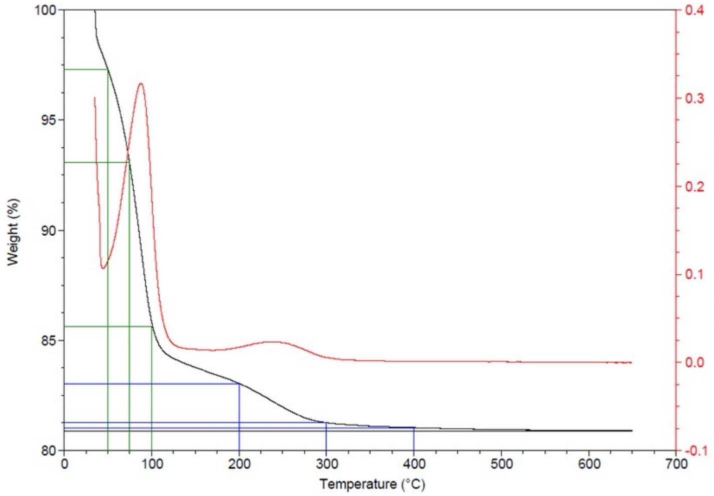

Figure S7. TGA profile of LTA(Li)-Ag_1 in which the different temperatures used for the *in-situ* experiments are marked with green and blue lines.

The vibrational dynamics of water molecules within zeolitic environments are strongly dependent on the host structure (zeolite topology and chemical composition). The water-water and water-zeolite framework interactions through hydrogen bonding and the water-extra framework cation interactions through ion-dipole interactions have been previously investigated by vibrational spectroscopy.[5,6] This technique has been employed to study differences in the chemical composition and/or in the topology of the analyzed zeolite by following the differences in the vibrational dynamical properties of the water molecules contained in such scaffolds. We utilized in this study this technique to complement the information obtained by TGA and EXAFS analysis.

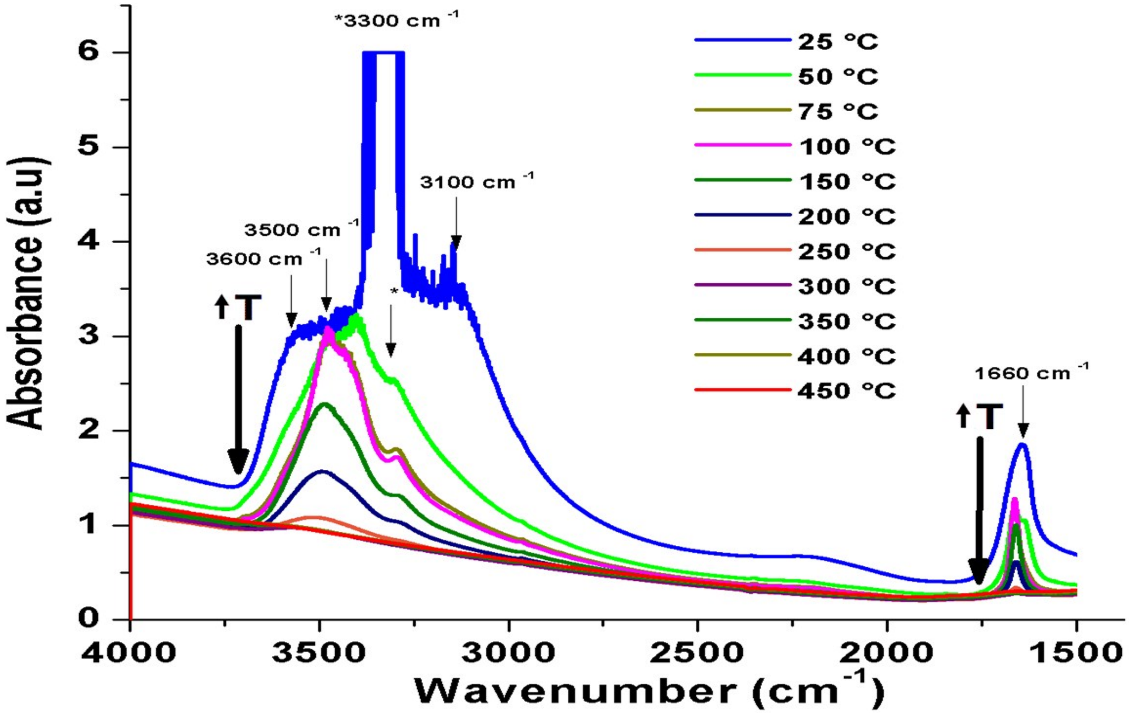

Figure S8. *In situ* temperature-dependent FT-IR measurements of LTA(Li)-Ag_1.

The temperature-dependent FT-IR spectra of LTA(Li)-Ag_1 under vacuum conditions measured from 25 to 450 °C are displayed in Figure S8. The IR bands between 2800 - 4000 cm^{-1} and between 1600 - 1700 cm^{-1} have been previously assigned to the OH stretching and HOH bending modes of water molecules in zeolites,[5-9] respectively. In this case, at room temperature, the OH band is very broad and could be tentatively related to four different contributions.[4-8] The first band at ~ 3100 cm^{-1} could be ascribed to the tetrahedral configuration of water molecules coordinated to extra framework cations, for instance, Na, Li, and Ag in this case. The second band centered around ~ 3300 cm^{-1} could be attributed to tetrahedrally coordinated water molecules linked together through linear hydrogen bonding, yielding structures similar to those of bulk water structures. The third band at ~ 3500 cm^{-1} could be related to water molecules non-tetrahedrally bonded, giving rise to distorted-like structures with less coordinated water molecules. The last band centered around ~ 3600 cm^{-1} could be associated to either water molecules with dimer coordination, establishing linear hydrogen bonds or possibly to water molecules linked to the LTA zeolite framework. At higher temperatures, the OH bands intensities decreased due to dehydration of the zeolite structure. The decreasing of the high frequency OH band, starting from 75 °C, could be related to the complete removal of weakly bound hydrogen (interfacial) water molecules. The general trend of slight down shift of the OH stretching bands from 75 to 250 °C, specially of the OH bands at 3296 and 3482 cm^{-1} to 3282 and 3471 cm^{-1}, respectively, has been already reported for LTA in its Na form, and were ascribed to the influence of extra framework cations when the interfacial water molecules are removed.[8] In this case, the down shift of frequency could be attributed to the stronger interactions of water molecules with Na, Li, and Ag species compared to the weak interaction between water molecules at high temperatures.

Contrary to the four OH stretching bands, the presence of a single HOH band of water bending vibration at ~ 1660 cm^{-1} showed that this mode does not contribute to the different degrees of connectivity of the water molecules. Similar to the OH stretching bands, the peak intensities of bending water molecules decreased proportionally with increasing the temperature up to 250 °C. After this temperature, the HOH bending of water band is almost flat up to 450 °C which is in good agreement with OH bands behavior described elsewhere for LTA(Na).[8] Also, a small shift of the HOH bending frequency from 1662 to 1658 cm^{-1} is observed between 75 to 250 °C. This shift can be related to the breaking of the hydrogen bonds between the highly coordinated water molecules produced by thermal motion generating less bonded water molecules.[9]

From TGA experiments we estimated the number of water molecules present in LTA(Li)-Ag_1 composites treated under different temperatures. Additionally, from FT-IR measurements we corroborated the water loss behavior, at different temperatures, observed in TGA experiments. Nevertheless, we also obtained information about the different coordinations of the water molecules within the zeolite framework. We noticed that at the beginning of the thermal treatment, water molecules weakly bonded to the zeolite framework were released preferentially, whereas at higher temperatures the strongly bonded water molecules coordinated to the extra-framework cations/clusters were liberated.

S5. *In situ* excitation-emission profiles measured on LTA(Li)-Ag_1 composites at different temperatures.

From the excitation-emission two-dimensional plots that were measured on LTA(Li)-Ag_1 at different temperatures, we selected 260 nm as excitation wavelength to display the effect of the temperature treatment and water content on the emission profiles of LTA(Li)-Ag_1 samples. Such profiles (displaying absolute values) are depicted in Figure S9. A 30 nm blue shift was observed in the emission profile of the samples measured at 50, 75 and 100 °C (560 nm) compared to those measured at room temperature (590 nm). Based on the analysis carried out by EXAFS, a nuclearity close to 4 was observed for the species related to green/yellow emissive samples. Additionally, the time-resolved measurements showed three decay components of 60 ps, 800 ps and 3.5 ns, respectively upon 266 nm excitation. At 200 °C a remarkable decrease of the 560 nm emission band intensity together with the appearance of two new emission bands at 470 and 390 nm was recorded. The appearance of the blue emission signal was further studied by EXAFS analysis indicating a decrease of the nuclearity of these species from 4 to 3 as compared to the yellow emitting samples. Moreover, a significant decrease of the decay times for the blue emitting samples was recorded. When higher temperatures were employed, 300 and 400 °C, a blue shift of the 470 and 390 nm emission bands to 450 and 375 nm, and an increasing of the 375 nm emission signal, was observed. Further thermal treatment at 450 °C resulted in a remarkable decrease of all emission signals compared to those observed in samples treated at lower temperatures (Figure S9-B).

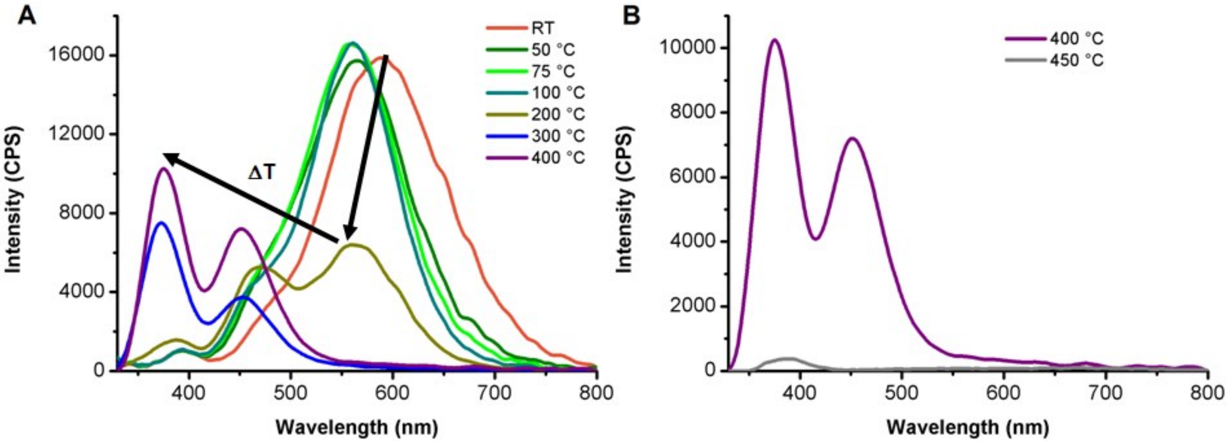

Figure S9. A) Emission profiles of LTA(Li)-Ag_1 at different temperatures, using 260 nm as excitation wavelength. B) Comparison of the emission profiles of LTA(Li)-Ag_1 at 400 and 450 °C (260 nm excitation), showing a large decrease of the luminescence signal in the sample treated at 450 °C.

To show the reversibility of the system, a series of hydration/dehydration cycles were performed on LTA(Li)-Ag_1 at room temperature and 400 °C, using 260 nm as excitation wavelength and monitoring the 450 and 590 emission bands (Figure S10-A). Additionally, in Figure S10-B a plot displaying the behavior of the system, when several hydration/dehydration cycles were performed on the sample is depicted. This demonstrates the reversibility of the system even after 10 hydration/dehydration cycles with no significant deviations of the emission profiles.

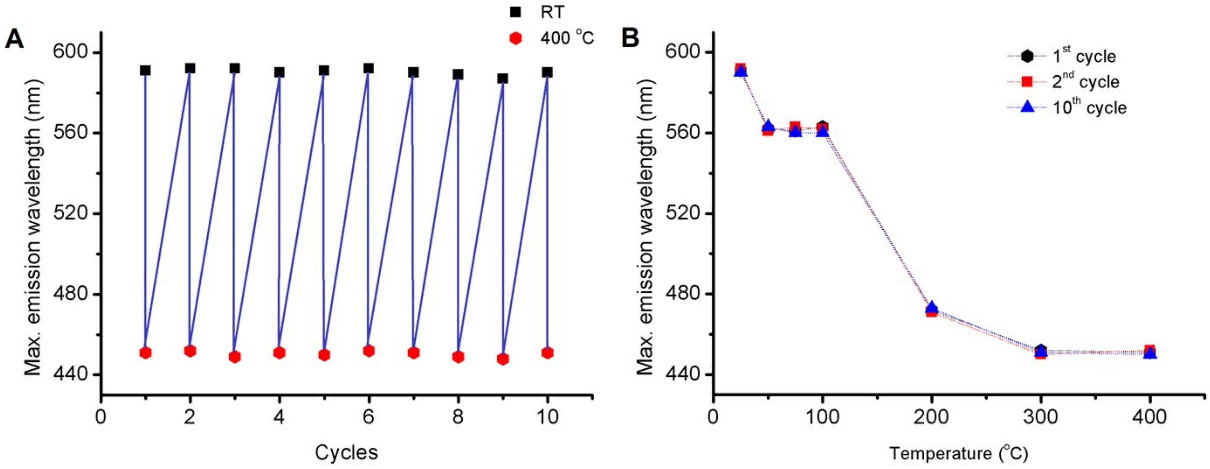

Figure S10. A) Emission maxima of LTA(Li)-Ag_1 at room temperature and 400 °C, during 10 hydration/dehydration cycles using 260 nm as excitation wavelength. B) Plot displaying the emission maxima profiles behavior of LTA(Li)-Ag_1 under different water contents after 10 hydration/dehydration cycles.

For the construction of the two-dimensional excitation-emission profiles of the luminescent LTA(Li)-Ag samples displayed in this study, the raw data was corrected for background and noise and interpolated to a resolution of 1 nm x 1 nm. In Figure S11 the 2D excitation-emission profiles of LTA(Li)-$Ag_{1,6,12}$ samples before and after interpolation are displayed. An improvement of the resolution of the excitation and emission profiles was achieved by performing the corrections and interpolations without altering the original features of the excitation-emission profiles.

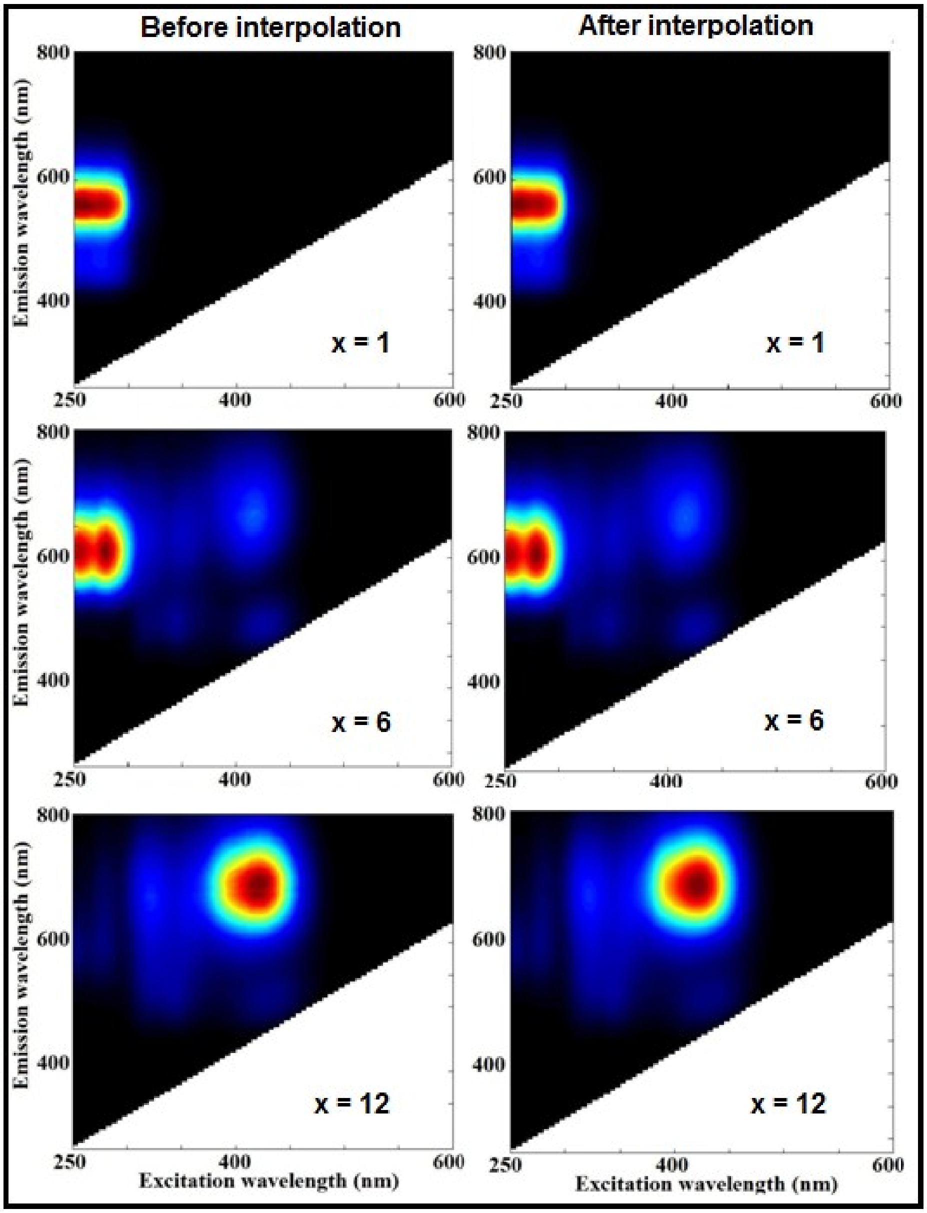

Figure S11.Two-dimensional excitation-emission plots of luminescent LTA(Li)-$Ag_{1,6,12}$ composites, in their fully hydrated state, before and after interpolation of the raw data.

S6. Diffuse reflectance (DRS) analysis of LTA(Li)-Ag composites. An UV-Vis-NIR Lambda 950 Perkin Elmer spectrophotometer equipped with a 150 mm diameter integrating sphere (coated with Spectralon) was used to record DRS spectra. The samples were placed in a Teflon sample holder and covered with a quartz plate for measurements.

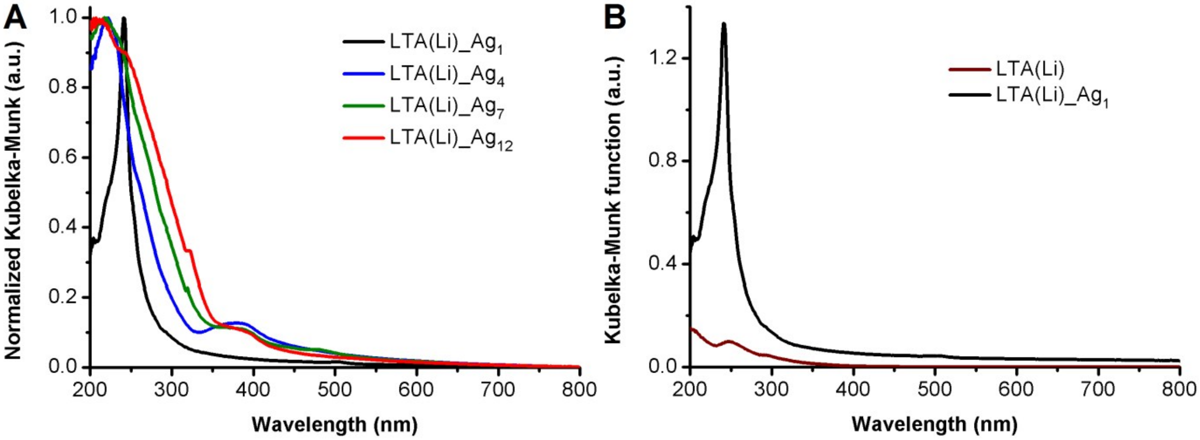

Figure S12. Kubelka-Munk spectra of A) LTA(Li)-Ag with different silver contents (Ag$_{1,4,7,12}$) and B) The starting material LTA(Li) compared to LTA(Li)-Ag$_1$.

The collected data were converted using the Kubelka-Munk formula. Kubelka-Munk spectra of non-exchanged LTA(Li) and silver exchanged LTA(Li)-Ag$_1$ zeolites are shown in Figure S12-B. No significant absorption bands in the spectrum of LTA(Li) were observed above 255 nm, whereas in the silver loaded LTA(Li) zeolites, absorption signals appeared in the UV and visible region. Such signals have been previously associated to silver atoms located at specific sites within the zeolite framework in silver exchanged LTA and FAU zeolites.[10]

S7. Luminescence decay measurements of LTA(Li)-Ag composites on the nano- and microsecond time scale.

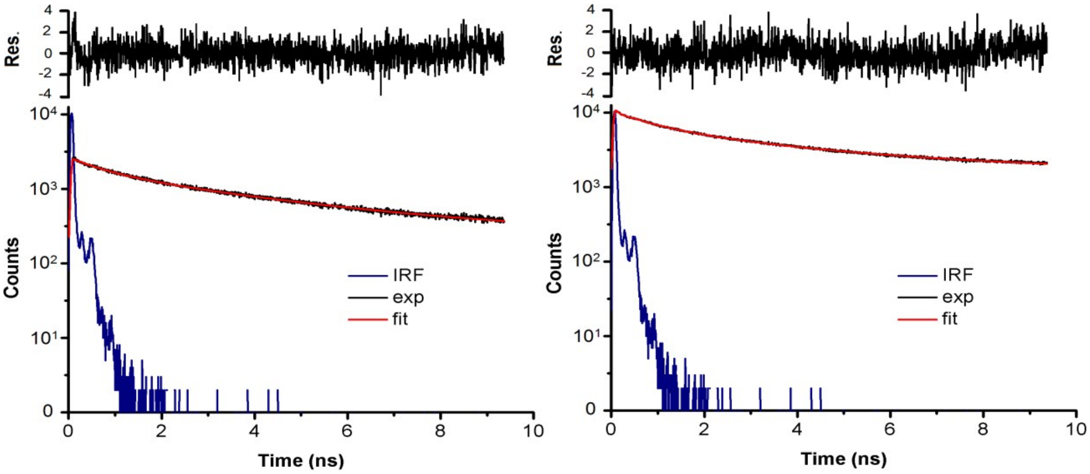

Figure S13. Nanosecond fluorescence decays and the corresponding fits and residuals, obtained by TCSPC of LTA(Li)-Ag_1 (left) and LTA(Li)-Ag_3 (right) samples in their fully hydrated state. Excitation and detection ocurred at 266 nm, and 580 nm respectively. The fitting parameters of the decay components are displayed in Table S3.

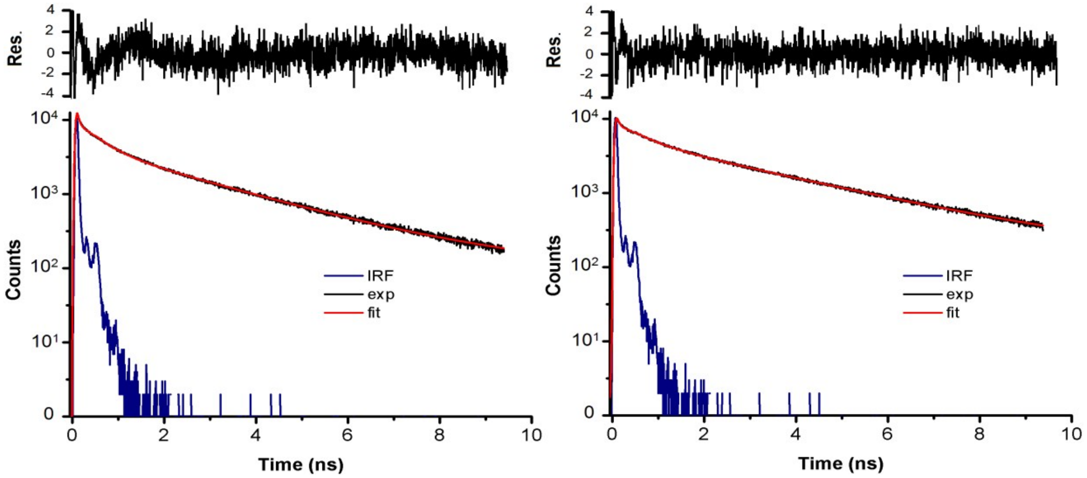

Figure S14. Nanosecond fluorescence decays and the corresponding fits and residuals, obtained by TCSPC of LTA(Li)-Ag_1 sample in its partially hydrated state. Excitation and detection ocurred at 266 nm and 390 nm (left plot), and 266 nm and 470 nm (right plot). The fitting parameters of the decay components are displayed in Table S4.

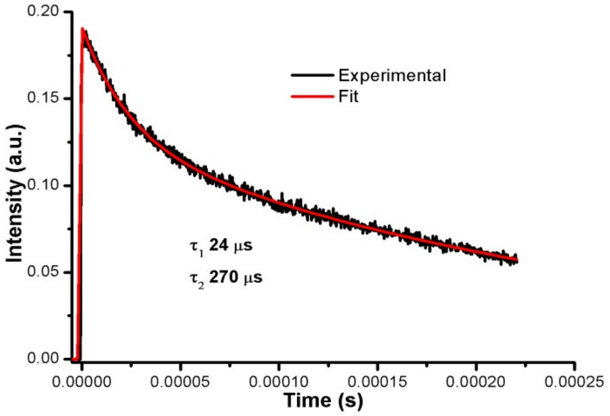

Figure S15. Microsecond luminescence decays and corresponding fits of LTA(Li)-Ag_1 in its fully hydrated state. Excitation and detection ocurred at 266 nm, and 580 nm respectively.

Table S3. Decay components and fitting parameters of the decay analysis of LTA(Li)-$Ag_{1\text{-}12}$ samples in their fully hydrated state.

Sample	**τ_1 (ns)**	**A1**	**τ_2 (ns)**	**A2**	**τ_3 (ns)**	**A3**	**χ^2**
266 nm excitation - 580 nm detection							
LTA(Li)_Ag1	0.054	0.008	0.892	0.111	4.163	0.881	0.967
LTA(Li)_Ag2	0.043	0.008	0.892	0.134	4.003	0.858	1.103
LTA(Li)_Ag3	0.057	0.009	0.828	0.133	3.813	0.859	1.117
LTA(Li)_Ag4	0.041	0.001	1.098	0.153	4.161	0.846	1.086
LTA(Li)_Ag5	0.058	0.012	0.591	0.117	2.964	0.871	1.045
LTA(Li)_Ag6	0.062	0.014	0.596	0.069	3.507	0.917	1.018
420 nm excitation - 685 nm detection							
LTA(Li)_Ag7	0.065	0.021	4.857	0.978			1.070
LTA(Li)_Ag8	0.108	0.031	5.090	0.968			1.103
LTA(Li)_Ag9	0.116	0.029	5.753	0.970			1.117

LTA(Li)_Ag10	0.090	0.035	5.265	0.964			1.096
LTA(Li)_Ag11	0.054	0.053	4.744	0.946			1.142
LTA(Li)_Ag12	0.041	0.106	4.960	0.893			1.174

Table S4. Decay components and fitting parameters of the decay analysis of LTA(Li)-$Ag_{1\text{-}4}$ samples in their partially hydrated state.

Sample	**τ_1 (ns)**	**A1**	**τ_2 (ns)**	**A2**	**τ_3 (ns)**	**A3**	**χ^2**
266 nm excitation - 390 nm detection							
LTA(Li)_Ag1	0.037	0.011	0.580	0.072	2.230	0.917	1.171
LTA(Li)_Ag2	0.042	0.029	0.408	0.164	2.218	0.807	1.102
LTA(Li)_Ag3	0.031	0.025	0.517	0.153	2.404	0.822	1.023
LTA(Li)_Ag4	0.028	0.049	0.433	0.193	2.064	0.758	1.064
266 nm excitation - 470 nm detection							
LTA(Li)_Ag1	0.034	0.009	0.480	0.065	3.279	0.925	1.042
LTA(Li)_Ag2	0.040	0.019	0.521	0.108	3.003	0.847	1.167
LTA(Li)_Ag3	0.037	0.019	0.607	0.179	2.922	0.802	1.144
LTA(Li)_Ag4	0.032	0.043	0.470	0.182	2.457	0.775	1.201

S8. Extended X-ray Absorption Fine Structure (EXAFS) analysis.

Table S5. Results of the curve fitting of Ag K-edge EXAFS refinements of LTA(Li)-Ag_1 composites with different hydration levels.

Samples	Pellet	Quartz cell	Capillary	Capillary
Hydration state	Fully hydrated (~19 % water content)	Partially dehydrated (~2 % water content)	Partially dehydrated (~1 % water content)	Fully Dehydrated
E_f (eV)	-3.5 (4)	-2.5 (8)	-5.4 (4)	-3.1 (4)
AFAC	0.9	0.9	0.9	0.9
k-range	2-12.8	2-12	2-12.5	2-12.4
N_1	1.3 (3) O	1.4 (9) O	1.3 (4) O	1.4 (1) O
R_1	2.29 (2)	2.28 (3)	2.31 (2)	2.305 (5)
A_1	0.014 (5)	0.018 (7)	0.015 (4)	0.021 (3)
N_2	2.7 (9) Si/Al	2.9 (12) Si/Al	2.7 (9) Si/Al	2.9 (6) Si/Al
R_2	3.22 (5)	3.22 (4)	3.28 (1)	3.22 (2)
A_2	0.06 (4)	0.03 (2)	0.026 (8)	0.017 (4)
N_3	1.7 (5) Ag	0.9 (7) Ag	1.0 (6) Ag	1.0 (2) Ag
R_3	2.81 (3)	2.58 (9)	2.58 (9)	2.782 (6)
A_3	0.031 (7)	0.07 (9)	0.07 (4)	0.020 (2)
N_4	1.4 (5) Li	1.1 (8) Li	1.4 (9) Li	1.2 (3) Li
R_4	2.98 (5)	3.02 (6)	3.05 (4)	2.88 (6)
A_4	0.002 (8)	0.005 (9)	0.009 (9)	0.011 (9)
N_5	1.3 (3) O	1.1 (8) O	0.7 (3) O	1.0 (5) O
R_5	2.45 (3)	2.47 (8)	2.44 (5)	3.22 (6)
A_5	0.014 (7)	0.03 (3)	0.017 (9)	0.007 (9)
N_6	0.2 (2) Ag	-	0.2 (1) Ag	0.6 (2) Ag
R_6	3.44 (5)	-	3.47 (3)	3.37 (2)
A_6	0.03 (2)	-	0.012 (7)	0.021 (9)
N_7	-	-	0.2 (1) Ag	1.1 (2) Ag
R_7	-	-	3.96 (3)	3.92 (1)
A_7	-	-	0.014 (9)	0.028 (6)
R (%)	27 %	40 %	25 %	17 %

E_f = contribution of the wave vector of the zero photoelectron relative to the origin of k [eV]
AFAC = amplitude reduction due to many-electron processes (AFAC fitting from Ag foil defined as 0.9)
N = number of atom in the N_i^{th} shell
R = radial distance of atoms in the N_i^{th} shell [Å]
A = Debye-Waller term of the N_i^{th} shell ($A=2\sigma^2$ with σ = Debye-Waller factor)[$Å^{-2}$]
R factor in %

Calculation of the coordination numbers of silver clusters in LTA(Li)-Ag_1 composites under different hydration levels. The second peak in the FT is a multipeak composed of an Ag-Si/Al contribution (N2) with a relatively stable distance varying from 3.22 to 3.28 Å among the four samples. Close inspection of the LTA crystalline structure (Figure S2) reveals that this Si/Al contribution might correspond to the fraction of the silver cations, which are not directly involved in the clusters nuclearity, that are located in the supercage above the center of the S6R (Figure S2) in LTA(Li) zeolites. These silver cations are strongly bonded to the three oxygen atoms of the zeolite ring pointing towards the center of the S6R at 2.30 Å which is in line with the Ag-O distance we obtained for the shortest Ag-O shell. This is further corroborated by the constant 2:1 ratio of the Al/Si and O shells coordination numbers we found in all samples corresponding exactly to the local environment of the cations situated at the centers of the SR6 (Figure S2). Implementing a dual O shell model in the first FT peak analysis allows obtaining an excellent agreement between the Ag-O and Ag-Si/Al distances and the O and Si/Al coordination numbers for the fraction of Ag cations that are isolated and directly bonded to the zeolite framework. Based on this information, we estimated the fraction of silver cations which are not directly involved in the clusters nuclearity, this fraction (2.7-2.9/6 Al/Si atoms in the S6R = 0.45 to 0.48) corresponds to ca. 45 - 48 % of the total number of silver cations originally exchanged in the zeolite framework.

In addition to the large Ag-Si/Al contribution an Ag-Ag contribution (N3) could also be detected in the second FT peak. In contrast with the other shells, the coordination and the bond distance of this Ag-Ag shell show large variations among the four samples investigated (fully hydrated, partially hydrated and fully dehydrated), and ranged from 2.81 to 2.58 Å and 1.7 to 0.9, for the bond distances and coordination, respectively. This contribution may correspond to the remaining part of the silver atoms (55 to 52%) forming oligomeric clusters located inside the sodalite cage (Figure S2). A calculation based on the silver coordination numbers of 3.1 (1.7/0.55), 1.6 (0.9/0.55), and 1.8 (1/0.55) suggests that the clusters nuclearity is about 4 in the hydrated sample, and close to 3 in the partially dehydrated samples and fully dehydrated material. The unusually large Debye-Waller factor associated with this Ag-Ag shell (from 0.02 to 0.07 Å^{-2}) demonstrates the large level of static disorder affecting most of these silver clusters.

Supporting video

Supporting Video S1: This video shows the as-prepared LTA(Li)-Ag$_1$ sample in his dehydrated state (at the beginning of the footage) with a quartz plate covering the central part of the powder displaying a blue emission when excited at 254 nm. As the sample starts to get hydrated (under ambient conditions) a gradual color change of the emission from blue to yellow is visualized at the regions where the powder is not covered by the quartz plate. In the second part of the video the quartz plate is removed allowing water to interact with the sample, resulting in the complete transformation of the emission color from blue to yellow under 254 nm illumination.

References

1) H. Yahiro, K. Kurohagi, G. Okada, Y. Itagaki, M. Shiotani, A. Lund, *Phys. Chem. Chem. Phys.* **2002**, *4*, 4255-4259.

2) H. S. Kim, D. Bae, W.T. Lim, K. Seff, *J. Phys. Chem. C* **2012**, *116*, 9009-9018.

3) H. S. Kim, S.Y. Choi, W.T. Lim, *J. Porous Mater.* **2013**, *20*, 1449-1456.

4) S. Leyre, E. Coutino-Gonzalez, J. Joos, J. Ryckaert, Y. Meuret, D. Poelman, G. Durinck, J. Hofkens, P. Hanselaer, *Rev. Sci. Instr.* **2014**, *85*, 123115(1-9).

5) V. Crupi, F. Longo, D. Majolino, V. Venuti, *J. Phys. Condens. Mat.* **2006**, *18*, 3563-3580

6) V. Crupi, F. Longo, D. Majolino, V. Venuti, *J. Chem. Phys.* **2005**, *123*, 154702.

7) S. Le Caer, S. Pin, S. Esnouf, Q. Raffy, J.P. Renault, J.B. Brubach, G. Creff, P. Roy, *Phys. Chem. Chem. Phys.* **2011**, *13*, 17658-17666.

8) P. Demontis, J. Gulin-Gonzalez, H. Jobic, M. Masia, R. Sale, G.B. Suffritti, *ACS Nano* **2008**, *2*, 1603-1614.

9) V. Crupi, D. Majolino, F. Longo, P. Migliardo, V. Venuti, *Vib. Spectrosc.* **2006**, *42*, 375-380.

10) R. Seifert, R. Rytz, G. Calzaferri, G. *J. Phys. Chem. A* **2000**, *104*, 7473-7483.